All-optical mapping of cAMP transport reveals rules of sub-cellular localization

Katherine M. Xiang[1], Pojeong Park[2], Shon A. Koren[3], Rebecca Frank Hayward[4], Adam E. Cohen[1,2*]

[1] Department of Physics, Harvard University
[2] Department of Chemistry and Chemical Biology, Harvard University
[3] Department of Neurobiology, Harvard Medical School
[4] School of Engineering and Applied Science, Harvard University
[*] cohen@chemistry.harvard.edu

Abstract

Cyclic adenosine monophosphate (cAMP) is a second messenger that mediates diverse intracellular signals. Studies of cAMP transport in cells have produced wildly different results, from reports of nearly free diffusion to reports that cAMP remains localized in nanometer-scale domains. We developed an all-optical toolkit, termed cAMP-SITES, to locally perturb and map cAMP transport. In MDCK cells and in cultured neurons, cAMP had a diffusion coefficient of ~120 $\mu m^2/s$, similar to the diffusion coefficients of other small molecules in cytoplasm. In neuronal dendrites, a balance between diffusion and degradation led to cAMP domains with a length scale of ~30 µm. Geometrical confinement by membranes led to subcellular variations in cAMP concentration, but we found no evidence of nanoscale domains or of distinct membrane-local and cytoplasmic pools. We introduce theoretical relations between cell geometry and small-molecule reaction-diffusion dynamics and transport to explain our observations.

Introduction

Cells must respond appropriately to diverse cues in their environment. In eukaryotic cells, external ligands can activate G protein-coupled receptors (GPCRs), triggering a second-messenger signaling cascade. There are approximately 800 GPCRs in the human genome (*1*), converging to only 5 canonical second-messenger pathways. The spatial spread of GPCR signals is thought to play a critical role in governing downstream effects (*2–4*). How does the influence of GPCR activation in one part of a cell spread through the rest of the cell, and how is this spread affected by cell geometry and by the arrangement of other molecules involved in the signaling cascade? Do signals remain localized in nanometer-size domains, or do they spread freely throughout the cell? Here we study the sub-cellular spread of the second messenger cyclic adenosine monophosphate (cAMP).

Spatial localization of cAMP signals has been proposed to play a key role in its signaling specificity (*4–8*), i.e. allowing two different GPCRs to signal through the same second messenger yet trigger different physiological responses within a single cell (*2–4*). In rat cardiomyocytes, β1-adrenergic receptor (AR) and β2-AR stimulation both generate cAMP, but trigger different downstream pathways (*4*, *5*, *9*). This effect has been explained by the fact that these two receptors localize to different subcellular regions (*10*) — β1-ARs localize to the entire cell surface as well

as the Golgi (*4*), while β2-ARs are confined to deep tubules. In zebrafish myocytes, cAMP generated in the primary cilium remains localized within the cilium and is differentially interpreted from extraciliary cAMP (*6*). In cells with extreme geometries such as neurons, diffusive transport can be heavily affected by asperities such as dendrites and their spines (*11–13*). Localized cAMP signaling may contribute to synaptic tagging (*14*), clustered plasticity (*15*), and differential effects of neuromodulators on cell excitability and gene expression (*16*). In these examples, the cAMP confinement is essentially geometrical: largely impermeable membrane boundaries create localized pools which have weak diffusive coupling to other compartments.

The sub-cellular propagation of cAMP also depends on the distributions of the many molecules with which it interacts. A-kinase anchoring proteins (AKAPs) scaffold together GPCRs with adenylyl cyclases (ACs) which produce cAMP, phosphodiesterases (PDEs) which degrade cAMP, and the downstream effector protein kinase A (PKA). Reversible binding of a small molecule to stationary or slowly diffusing binding partners can substantially impede subcellular transport. This "buffered diffusion" has been studied in detail for Ca^{2+} (*17–20*), and similar principles apply to cAMP (*21*). Furthermore, feedback between cAMP and Ca^{2+} signaling pathways can affect dynamics in space and time (*22*). Due to the dependence of cAMP transport on nanoscale molecular arrangements and on incompletely known interaction parameters, the rules of cAMP transport in cells must be characterized experimentally.

Recent work suggested that nanometer sized cAMP domains exist around individual receptor molecules (*23*), and that these achieve downstream specificity by acting on locally tethered PKA. A key challenge for this model is that molecular-scale cAMP localization requires cAMP diffusion to be at least 100-fold slower than in free solution and/or PDE rate constants to be at least 100-fold higher than measured *in vitro* (Supplementary Materials). It is unclear how these effects could occur. Estimates of cAMP diffusion in cells have varied by ~100-fold, from 5 $\mu m^2/s$ (*24*) to 780 $\mu m^2/s$ (*25*), but direct measurements of diffusion have been challenging.

To determine the rules governing cAMP transport and to test predictions of nanoscale localization, we set out to map cAMP transport in cells. We developed bicistronic constructs to co-express a blue light-activated adenylyl cyclase, bPAC (*26*), with a yellow-excited fluorescent cAMP reporter, Pink Flamindo (*27*), with distinct sub-cellular localization tags on the two proteins. We call these tools "cAMP Sub-cellular Indicators of Transport", or cAMP-SITES.

By combining sub-cellular molecular and optical targeting, we probed cAMP transport over length scales from nanometers to ~100 μm. We found that cAMP diffused relatively freely in MDCK cells and in neurons, with a diffusion coefficient of ~120 $\mu m^2/s$. Neuronal dendrites supported cAMP "domains" of ~30 μm, set by the balance of diffusion and degradation. We found no evidence of nanoscale domains or of a separate membrane localized pool. cAMP concentrations were strongly affected by local surface-to-volume ratio, and whether production and degradation each occurred in solution or on the membrane. We introduce scaling rules which relate cell geometry to the localization and spread of soluble signals and compare to the spread of electrical signals.

Results

An all-optical toolkit for studying cyclic AMP transport.

To enable independent optical perturbation and measurement of cAMP in cells, we first created the cAMP-SITE construct CMV::PinkFlamindo-p2a-bPAC (hereafter, PF+bPAC), where p2a is a self-cleaving peptide linker (Fig. 1A). Blue (488 nm) light activated the bPAC to drive cAMP production. Yellow (561 nm) light excited Pink Flamindo (PF) fluorescence to probe the cAMP dynamics. To achieve sub-cellular control of bPAC activation, we used a digital micromirror device (DMD) to pattern the blue light with micron-scale precision (Fig. 1B, Methods). After a brief (0.5 s) pulse of patterned blue light delivered to a field of HEK293T cells, PF fluorescence increased in the illuminated regions over ~40 s, and then returned to baseline over several minutes (Fig. 1C). Similar dynamics were observed when bPAC was activated in subcellular domains in MDCK cells (Fig. 1C). In this case the cAMP signal gradually diffused out of the directly stimulated regions but remained within the contours of the stimulated cells.

As blue light dose increased, the peak PF fluorescence response increased linearly and then saturated at $\Delta F/F = 1.8 \pm 0.2$ ($n = 38$ cells, mean ± s.d., Fig. 1D–E), with a half-maximal response at a blue illumination dose of $I_{1/2} = 24 \pm 5$ μJ/mm^2. Treatment with 100 μM forskolin, a broad-spectrum AC activator, and 200 μM IBMX (3-isobutyl-1-methylxanthine, a broad-spectrum PDE inhibitor) did not increase the PF $\Delta F/F$ beyond the level induced by saturating blue light (Fig. S1A), implying that the saturation behavior observed in Fig. 1E was likely PF saturation. The relation between optical dose and cAMP production depends on the expression level of bPAC, so the value of $I_{1/2}$ could vary between cell types and experimental conditions. To avoid saturating the PF reporter, we adjusted blue light doses to keep $\Delta F/F < 1$ for subsequent experiments.

We performed pharmacological tests to confirm that PF was reporting cAMP (Table 1). In HEK cells expressing PF+bPAC, rolipram, a PDE4 inhibitor, enhanced the magnitude and duration of the PF response to a blue light pulse (Fig. 1F). In separate experiments, MR-L2, a PDE4 activator, decreased the magnitude and duration of the PF response. Control experiments in HEK cells expressing just PF showed no response to blue excitation (Fig. 1F), confirming that the blue light did not disturb the PF mApple chromophore or perturb cAMP through pathways independent of bPAC. HEK cells expressing PF+bPAC but exposed only to steps of yellow light did not show cAMP transients, confirming that the yellow imaging light did not drive spurious bPAC activation (Fig. S1B). Together, these experiments established that the PF+bPAC pair enabled crosstalk-free all-optical perturbation and measurement of cAMP dynamics in cells.

All-optical measurements of PDE kinetics.

To help interpret quantitative measurements of cAMP dynamics and transport, we constructed a kinetic model for bPAC activation and the cAMP response (Fig. 2A) and derived expressions for the change in cAMP concentration as a function of time (Supplementary Materials).

We considered the response to a brief blue light pulse, of duration short compared to the bPAC relaxation. After this pulse, the concentration of the bPAC activated state (bPAC*)

followed an exponential decay with rate constant $k_{\mathrm{rev}}^{\mathrm{bPAC}}$. We assumed that cAMP production is first order in bPAC*, that substrate (ATP) is in excess; and that cAMP degradation is first order in cAMP and first order in PDE concentration, with rate k_{PDE}. We assumed that PF binding to cAMP equilibrates fast compared to changes in cAMP concentration, that the cAMP concentration is within the linear response range of the PF, and that the PF does not substantially buffer the cAMP. This model fit well to the PF+bPAC data in HEK cells (Fig. 2B).

We then produced versions of the cAMP-SITEs where one or both of the bPAC and the PF were targeted to the membrane. The goals were (a) to minimize diffusion of the source (bPAC) as a confounding variable in measurements of cAMP transport, (b) to investigate the possibility of distinct cAMP pools at the membrane vs in the cytoplasm, and (c) to develop a toolkit to explore the interaction of source localization and cell geometry on cAMP transport and dynamics. We generated four cAMP-SITEs to co-express all combinations of soluble and membrane bound PF and bPAC (Fig. 2C, Fig S2) and designated these: PF+bPAC, PF+bPAC^{m}, PF^{m}+bPAC, and PF^{m}+bPAC^{m} (Table 2). The p2a linker left 21 amino acids on the C-terminus of the first protein in each sequence (*28*) and was incompatible with the also C-terminal CAAX membrane-targeting motif. We used the CAAX motif to target bPAC to the membrane and an N-terminal myristoylation motif (*29*) to target PF to the membrane (Methods).

We confirmed that PF^{m} was membrane bound by directly imaging its fluorescence (Fig. 2D). For bPAC^{m}, we attached a GFP tag and confirmed its membrane localization (Fig. 2D). To probe the lateral diffusion of bPAC^{m}, we expressed a fusion of photoactivatable GFP (paGFP) to bPAC^{m} and used patterned illumination at 405 nm to activate the paGFP in a sub-cellular region. We compared the diffusive spread of paGFP-bPAC^{m} to that of soluble paGFP-bPAC (Fig. S3, Methods). The membrane bound bPAC showed little diffusion over the 100 s timescale of our measurements, while the soluble bPAC spread freely: for paGFP-bPAC^{m}, after 25 s only 5% of the fluorescence (quantified by ΔF) had spread outside the photoactivated region. For the soluble paGFP-bPAC, 25% of the fluorescence had spread during the same time interval (n = 3 cells for each construct).

We transiently expressed all four cAMP-SITE constructs in HEK cells, delivered a wide-area blue light pulse (0.5 s, 10–21 μJ/mm^2) to activate bPAC, and recorded the PF fluorescence responses (Fig. 2E). We fit the cell-average ΔF/F traces to our kinetic model (Methods) and found that for all constructs, $1/k_{\mathrm{rev}}^{\mathrm{bPAC}} \approx 20$ s, consistent with prior *in-vitro* measurements (*26*, *30*). We also found that $1/k_{\mathrm{PDE}} \approx 60$–80 s for all combinations of membrane-bound and soluble bPAC and PF (Table 3). These results suggest that there are not distinct pools of membrane-associated or soluble cAMP, but rather that the cAMP is well mixed throughout the cell on the timescale of 60 s (Fig. 2F).

Cyclic AMP diffuses freely in the cytoplasm with $D \approx 120$ μm^2/s.

Full mixing of cAMP across a ~10 μm cell in ~1 min could only occur if the cAMP diffusion coefficient in the cytoplasm obeyed $D >> 1$ μm^2/s. We thus sought to measure D for cAMP directly. We switched from working with HEK cells to MDCK cells because the latter often have a long

and thin geometry, which allowed us to approximate cAMP transport as a 1-dimensional process. We expressed the cAMP-SITE construct PF^m+$bPAC^m$, selecting the membrane-bound bPAC to minimize diffusion of the cAMP source, and the membrane-bound PF to avoid dependence of the baseline fluorescence on cell thickness. Using the DMD, we transiently activated $bPAC^m$ in a micron-scale region near one end of the cell, and then mapped the PF^m response (Fig. 3A–B). The PF^m fluorescence initially rose near the activated bPAC and then spread throughout the cell over ~30 s.

We augmented our kinetic model with a 1-D diffusion term for cAMP, leading to a four-parameter reaction-diffusion model which described the cAMP profile in time and space (Supplementary Materials). We performed a global fit of the model to the PF fluorescence dynamics over space and time within each cell, floating the three kinetic parameters and the diffusion coefficient. We found that the cAMP diffusion coefficient was 130 ± 40 $\mu m^2/s$, mean ± s.d., n = 5 cells (Fig. 3C). We performed the same measurement in dendrites of cultured rat hippocampal neurons (Fig. 3D) and found that the diffusion coefficient was similar, 110 ± 30 $\mu m^2/s$, mean ± s.d., n = 25 neurites, 8 cells (Fig. 3E).

These results are consistent with other measurements of free diffusion of small molecules in cytoplasm (*31*, *32*), implying that cAMP diffuses relatively freely in the cytoplasm of MDCK cells and neurons. The peak $\Delta F/F$ remained < 1, even in the regions closest to the bPAC activation, ensuring that the PF^m response did not saturate and that the cAMP concentration remained < 10 μM, based on the published dose-response curve of Pink Flamindo (*27*).

cAMP is geometrically compartmentalized in membrane asperities and neurites.

We next explored the interaction of cell geometry, biochemistry, and cAMP reaction-diffusion dynamics. The AC sources of cAMP can be membrane-bound or soluble (*33*). For example, GPCRs can signal either from the membrane or after becoming internalized (*34*, *35*). The PDE sinks of cAMP can also be membrane-bound or soluble, and individual cells might have different isoforms of PDEs that are active at different cAMP concentrations (i.e. have different Michaelis constants K_m) (*22*, *36–38*). Membrane-bound enzymes (AC or PDE) have a higher effective concentration in regions of higher surface-to-volume ratio, even if homogeneously distributed and homogeneously activated throughout the cell membrane. The balance between membrane vs. soluble AC and membrane vs. soluble PDE could favor cAMP buildup either in regions of high or low surface-to-volume ratio. This same balance also affects how the length-scale of cAMP spread from a point source scales with surface-to-volume ratio.

To test these ideas experimentally, we compared the effects of $bPAC^m$ vs. bPAC in cultured rat hippocampal neurons (Fig. 4A). In neurons expressing PF^m+$bPAC^m$, illumination with a wide-area pulse of blue light (0.5 s, 21 – 83 $\mu W/mm^2$) led to larger peak cAMP concentrations in the dendrites than in the soma (Fig. 4B–D). We interpret this finding as a consequence of the higher effective concentration of $bPAC^m$ in the dendrites, due to their higher surface-to-volume ratio compared to the soma. We computed the ratio of the peak $\Delta F/F$ in each dendrite to the peak $\Delta F/F$

in its corresponding soma (Fig. 4H). For bPAC^m cells, $(\Delta F/F_{dendrite})/(\Delta F/F_{soma}) = 1.6 \pm 0.85$, mean ± s.d., n = 62 dendrites, 6 neurons. We chose to characterize the peak since it occurred at ~10 s post-stimulus, which was before diffusive spreading smoothed out transient cAMP concentration imbalances.

In contrast, for neurons expressing soluble bPAC (PF^m+bPAC), the same illumination and analysis protocol led to a larger PF^m signal in the soma than in the dendrites (Fig 4E–G) with $(\Delta F/F_{dendrite})/ (\Delta F/F_{soma}) = 0.75 \pm 0.22$, mean ± s.d., n = 33 dendrites, 6 neurons. The difference in this quantity between cells expressing bPAC and bPAC^m was significant (P = 1.0e-8, Wilcoxon rank-sum test). In cells expressing soluble bPAC, the greater cAMP signal in the soma than dendrites can plausibly be explained by at least a portion of the PDE activity being membrane bound and thus more active in the dendrites than in the soma.

We then studied the interchange of cAMP between dendrites and the soma. In neurons expressing PF+bPAC^m, we used patterned blue light (0.5 s, 83 μJ/mm^2) to activate cAMP production in a dendrite, and we mapped the distribution of cAMP along the line spanning from the dendrite to the middle of the soma (Fig. 4I). The change in cAMP concentration declined smoothly to approximately zero at the junction of the dendrite and the soma, a consequence of the comparatively large volume of the soma causing dilution of cAMP sourced from the dendrite. Essentially, the soma acted as an absorbing boundary at the junction with the dendrite.

We then patterned the blue light to activate cAMP production in the soma of the same cell. In this case, the cAMP propagated ~20 μm into the dendrites. The soma was able to source cAMP to the dendrites with minimal dilution of the source (Fig. 4J). Hence cAMP transport is asymmetric (Fig. 4K) with the soma influencing the proximal dendrites more than the proximal dendrites influenced the soma, a simple consequence of the different volumes of these structures. For distal dendrites, the increased volume in regions toward the soma as well as the branching structure of the dendritic tree could further compartmentalize cAMP signals.

The cAMP length constant varies between neurites, but does not show clear dependence on diameter

Finally, we measured the characteristic length scale for cAMP transport in neuronal dendrites, set by the balance of cAMP diffusion and PDE-mediated degradation (Fig. 5A). In cultured neurons expressing PF^m+bPAC^m, we repeatedly targeted the blue light to a small patch of dendrite and mapped the cAMP concentration until it reached steady state (Fig. 5B–D). We fit the steady state concentration profiles to an exponential decay vs. position (Fig. 5E) and extracted the length constants for neurites with diameters ranging from ~0.5 to 6 μm (Fig. 5F). The length constant was 27 ± 13 μm (mean ± S.D., n = 67 measurements), and did not show clear correlation with dendrite diameter. Neural activity (induced by elevated external KCl, Fig. S4) did not measurably affect the length scale.

Scaling relations for small-molecule transport in cells.

To understand how surface-to-volume ratio affects cAMP transport, we consider cAMP dynamics in a linear tube with diameter d and length L ($d \ll L$), and restrict attention to length scales $|x| > d$, so we can approximate the cAMP concentration by a one-dimensional profile $c(x)$ (i.e., neglecting transverse concentration gradients). The reaction-diffusion dynamics with constant production and first order degradation are:

$$\frac{dc}{dt} = D\frac{d^2c}{dx^2} + k_F - k_{PDE}c \qquad [1]$$

where c is the concentration of cAMP, D is the diffusion coefficient. The rate of cAMP production is $k_F = k_{cat}^{AC}[AC]$, which could vary with position and depends on the concentration of active adenylyl cyclase, [AC]. The adenylyl cyclase concentration refers to active enzymes, e.g. bPAC*. The rate of cAMP degradation is $k_{PDE} = \frac{k_{cat}^{PDE}}{K_m^{PDE}+[cAMP]}[PDE] \approx \frac{k_{cat}^{PDE}}{K_m^{PDE}}[PDE]$, assuming first-order Michaelis-Menten kinetics, which depends on the concentration of active phosphodiesterase, [PDE]. k_{cat} and K_m are the catalytic and Michaelis constants for their respective reactions (Supplemental Materials). For soluble enzymes, the enzyme concentration is independent of the tube diameter, while for membrane-bound enzymes, the effective concentration is $4\sigma/d$, where σ is the density per-unit membrane area.

For spatially homogeneous AC and PDE activities, the diffusion term in Eq. 1 is zero, and the steady-state concentration is $c = k_F/k_{PDE}$. Depending on whether the AC and PDE are each soluble or membrane localized, the numerator and denominator of this expression could each implicitly depend on tube diameter, d. The relative localization of AC and PDE could favor cAMP accumulation in either large or small-diameter tubes (Fig. 6A), consistent with our comparison of cAMP production via bPAC vs. bPAC^m in dendrites. The time constant τ to reach steady-state scales as d^1 for membrane-bound PDE, is independent of d for soluble PDE, and does not depend on whether the AC is soluble or membrane bound (Supplementary Materials).

For spatially localized AC activation, we model the AC as a stationary and continuously active source centered at $x = 0$, with small width Δx. The steady state cAMP concentration profile then decays exponentially away from the source:

$$c(x) = c_o e^{-\frac{|x|}{\phi}} \qquad [2]$$

where the prefactor $c_0 = \frac{k_F\,\Delta x}{2\sqrt{Dk_{PDE}}}$ is the amplitude of the response. The length $\phi = \sqrt{D/k_{PDE}}$ is the characteristic cAMP length scale and is known as the Thiele length (*39*). The Thiele length ϕ is the average distance that a molecule of cAMP diffuses before it is degraded. Here we assume $\phi \gg d, \Delta x$.

Both ϕ and c_0 depend on whether the AC and PDE are each membrane-bound or soluble, and on the tube diameter, d (Fig. 6B). The Thiele length does not depend on whether the AC is

soluble or membrane-bound because, by construction, the diffusion and degradation happen away from the region of AC activity. If the degradation occurs on the membrane, then $\phi \propto d^{1/2}$; if the degradation is in solution, then $\phi \propto d^0$. We did not observe clear diameter-dependent scaling in our measurements of ϕ (Fig. 5F). This discrepancy is possibly because the PDE was neither purely soluble nor purely membrane-bound, possibly due to heterogeneous sub-cellular distributions of PDE activity, and possibly because the presence of dendritic spines led to a more complex scaling of surface-to-volume ratio with diameter than for a simple tube.

For membrane-bound PDE, the scaling of peak concentration, c_0, with d is different for a point vs. homogeneous AC source (compare Fig. 6A and 6B, left). This non-intuitive result highlights the importance of the spatial structure of the activation, not just of the geometry of the cell. Remarkably, the area under the concentration vs. position curve (i.e. the spatial integral of Eq. 2) has the same scaling for point- and distributed sources. This can be seen by noting that the product $c_0 \times \phi$ for a point-source has the same d scaling as does the steady-state concentration for a distributed source.

Eq. 1 has the same mathematical structure as the cable equation for propagation of membrane voltage (*19*, *20*, *40*). However, the dependence of the parameters on tube diameter can be different. In the electrical case, current sources and sinks are always across the membrane, and so the scaling rules are the same as for the case where AC and PDE are both membrane-bound. The electrical length constant $\lambda = \sqrt{R_m d/4R_i} \propto d^{1/2}$, where R_m is the membrane resistivity and R_i is the axial resistivity. Typically electrical length constants in dendrites are $\lambda > 150$ μm (*41*, *42*), longer than most chemical signaling lengths. However, if the PDE is soluble, then $\phi \propto d^0$ and has different scaling with d compared to $\lambda \propto d^{1/2}$. Then there is, in principle, a crossover point where chemical signaling becomes longer-range than electrical signaling. If we posit a 5-fold difference between λ (~150 μm) and ϕ (~30 μm) at $d = 5$ μm, then a 25-fold decrease in d would be required to achieve parity (assuming purely soluble PDE activity). A diameter of 200 nm is attainable in cilia and cytoskeleton-free membrane tubes (*43*), but otherwise is outside the physiologically relevant range.

Some elements of the ideas presented here have been explored theoretically and experimentally with several diffusible messengers (*44–46*). Zador and Koch derived the diameter-dependent expressions for Ca^{2+} dynamics with transmembrane influx and efflux, and diffusible buffers; and drew analogy to the cable equation (*19*). Neves et al. and Castro et al. showed that bath application of low-concentration isoproterenol, a β-adrenergic receptor agonist, elevated cAMP preferentially in thinner neurites (*16*, *47*), presumably due to membrane-localized AC and predominantly soluble PDE. Bacskai et al. also observed a cAMP concentration gradient between the neurites and the soma of an *Aplysia* sensory neuron, upon uniform bath application of 5-HT (*25*). We are not aware of a prior presentation of the scaling relationships in Fig. 6, comparing all combinations of soluble vs. membrane-bound sources and sinks, and comparing point-like vs. distributed sources.

Discussion

Some have argued that cAMP diffuses relatively freely in cells (*48–50*), while others have suggested that highly restricted or buffered diffusion generates nanoscale compartments (*21*, *51*), and that individual GPCRs with closely coupled downstream effectors can function independently of other GPCRs (*23*). Using patterned cAMP production, we observed transport of cAMP from a spatially localized source and made quantitative measurements of its diffusion and transport lengths. We compared membrane-bound and soluble combinations of actuator and reporter and found little difference between the constructs in cAMP degradation kinetics or transport. We found no evidence of nanoscale compartmentalization or of nanoscale-localized cAMP sinks.

We propose that cAMP differential signaling is primarily governed by membrane-delimited compartmentalization in sub-cellular domains, combined with differential scaling of soluble vs. membrane-bound enzyme activities as a function of local surface-to-volume ratio. In neurons expressing $bPAC^m$, uniform stimulation favored cAMP accumulation in thin dendrites, but in neurons expressing soluble bPAC, uniform stimulation favored accumulation in the soma.

The length scale of cAMP transport in neurons (~30 μm) was short enough that cAMP remained compartmentalized in individual dendrites. Therefore, it is plausible that individual portions of the dendritic tree could experience localized neuromodulatory effects, possibly mediating local changes in dendritic computations or plasticity rules. The length scale of cAMP transport is in between that of Ca^{2+} (predicted to be several microns) (*19*, *20*) and membrane voltage (typically ~150 μm) (*41*, *42*). Further, our results show that drugs that differentially target membrane-bound versus soluble PDE (or AC) populations have potential to modulate the size and concentration of cAMP domains and therefore to have differential effects on downstream signaling.

The cAMP-SITES tools we developed here could be broadly useful for studying sub-cellular and intercellular cAMP transport. For example, the bPAC and the Pink Flamindo could be independently localized to different regions, such as mitochondria, nucleus, dendritic spines or flagella; one could thereby probe cAMP transport between any two of these regions. The bPAC and Pink Flamindo could also be expressed in adjacent cells, permitting studies of cAMP transport through gap junctions. The cAMP-SITES provide a convenient and robust assay of PDE activity, which may have use in high-throughput drug or genetic screens (*52*).

The effects of surface-to-volume ratio discussed here apply broadly to other small molecules and to systems where interacting partners are localized differentially on the membrane versus in the bulk (*46*, *53*, *54*). An important goal for future research will be to characterize the diffusion coefficients, length constants, and time constants for other signaling molecules. There exists a large and rapidly growing toolkit of spectrally distinct optogenetic perturbation tools and fluorescent reporters (*55–60*), and finding compatible pairs will open new windows into the spatial aspects of sub-cellular signaling.

Acknowledgments

We thank Andrew Preecha and Shahinoor Begum for technical assistance. This work was supported by a Hertz Foundation Fellowship (KX), the NSF Graduate Research Fellowship

Program under Grant #2140743 and #1745303 (KX), and a Vannevar Bush Faculty Fellowship (AEC).

Declaration of Interests

The authors declare no competing interests.

Supplemental Information

Quantitative modeling of cAMP kinetics and diffusion.

Figures

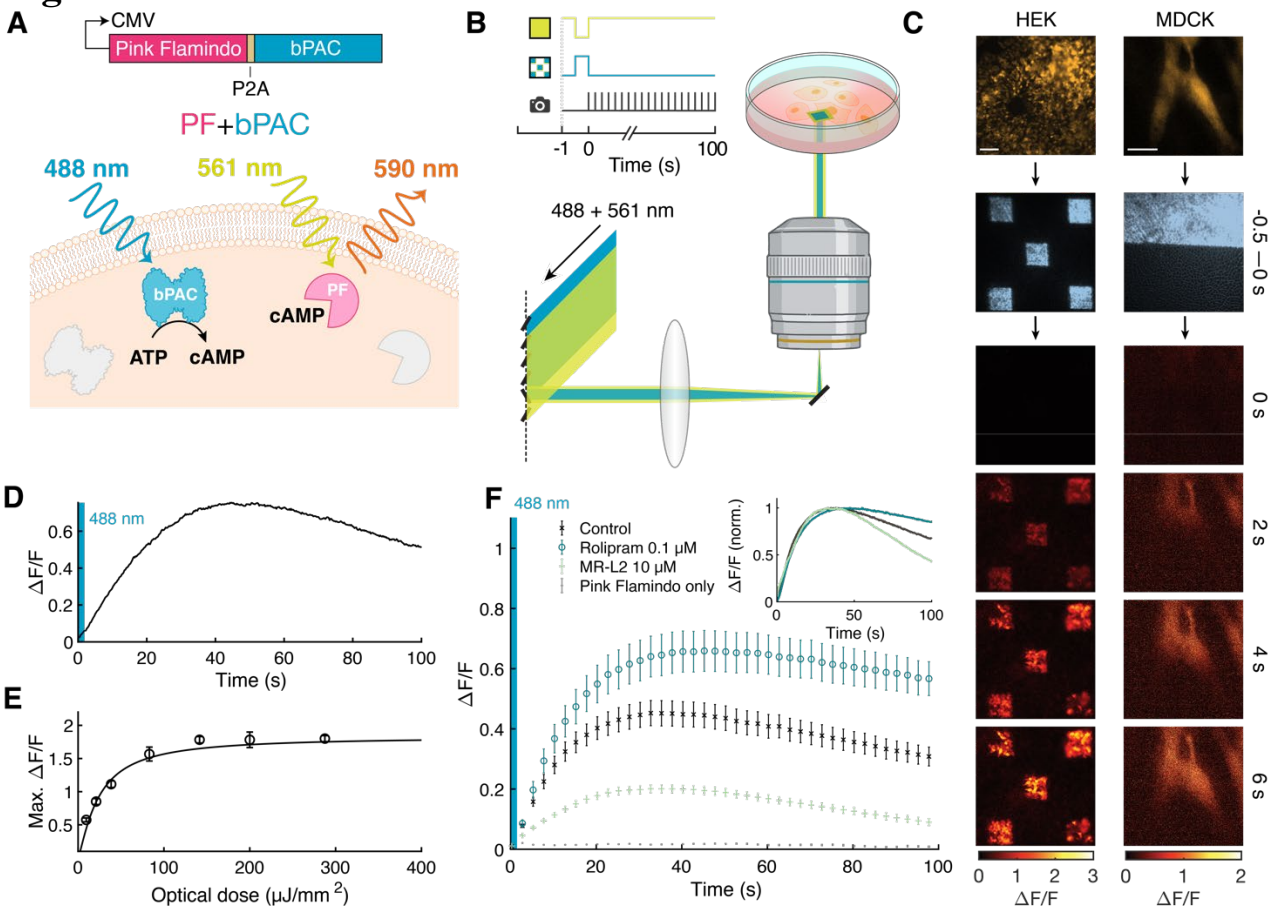

Figure 1. Targeted optogenetic production and measurement of cAMP.
A) Genetic construct for optogenetic production and imaging of cAMP. **B)** Illumination protocol for patterned optogenetic activation of bPAC (blue, 488 nm, 0.5 s), followed by wide-field imaging of PF (yellow, 561 nm). **C)** Top: basal PF fluorescence in a dish of HEK cells (left, scale bar: 100 μm) and MDCK cells (right, scale bar: 20 μm) expressing PF+bPAC. Middle: Patterns of transient (0.5 s) blue illumination for bPAC activation. Bottom: images of PF ΔF/F at 2-s intervals show subsequent cAMP dynamics. Note intracellular spread of cAMP away from the blue-illuminated region in the MDCK cells. **D)** Example single-cell ΔF/F trace in a HEK cell. **E)** Blue light dose-response curve of PF+bPAC, measured by peak ΔF/F. Fit to Hill equation gives saturating ΔF/F = 1.8 ± 0.2 (mean ± s.d.), half-saturating blue light intensity 24 ± 5 μJ/mm^2, and Hill coefficient 1.2 ± 0.3 (95% CI from the computed Jacobian, n = 11 – 60 cells per data-point. Error bars represent SEM.) **F)** Response of HEK cells expressing PF+bPAC subject to the protocol in (D) with 21 μJ/mm^2 blue light (black, n = 40 cells from 3 dishes). Cells treated with the PDE inhibitor rolipram (blue, n = 19 cells from 2 dishes) had slower recovery and larger peak ΔF/F. Cells treated with the PDE activator MR-L2 (green, n = 39 cells from 2 dishes) had faster recovery and smaller peak ΔF/F. Cells expressing PF without bPAC (gray, n = 42 cells from 2 dishes) did not respond to blue light. Inset: peak-normalized traces. Error bars represent SEM.

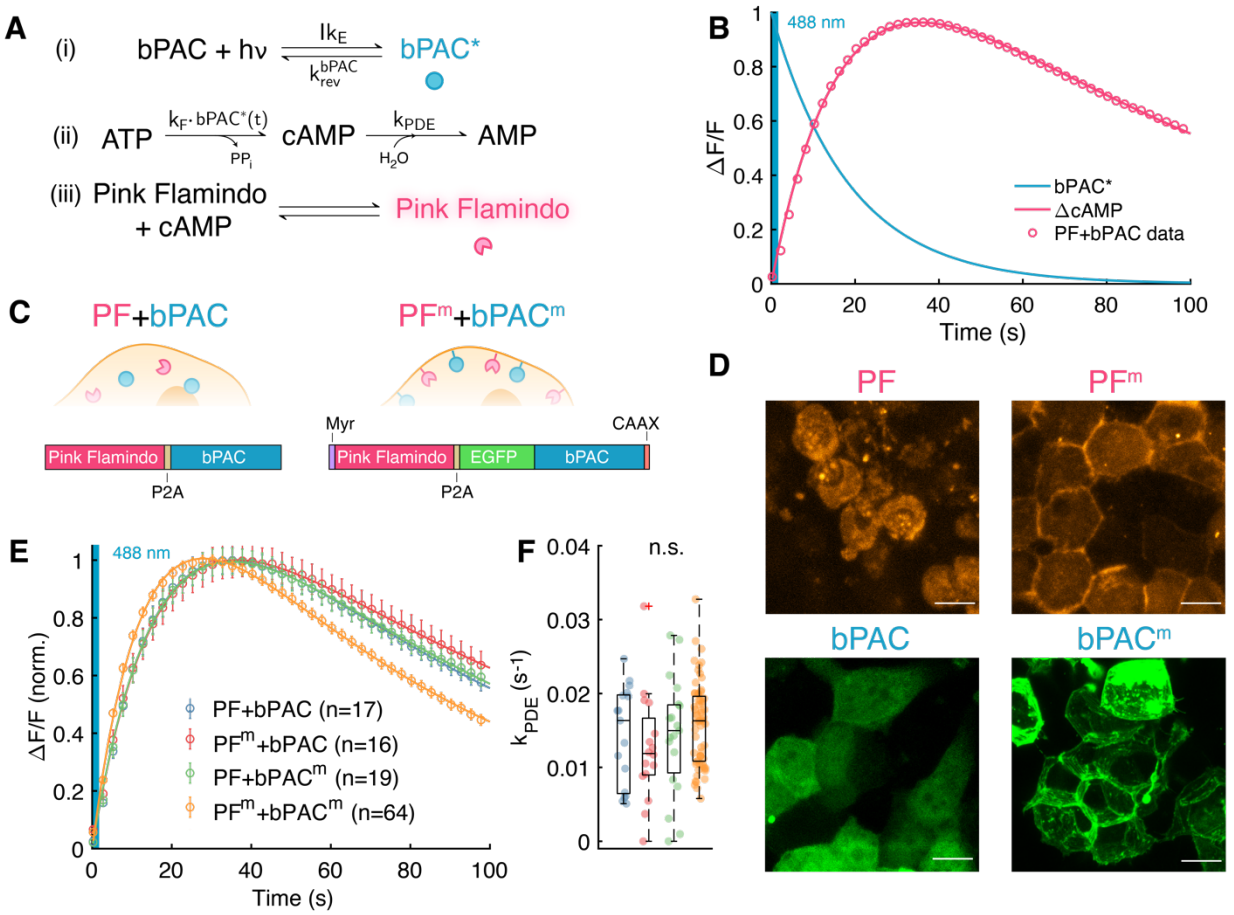

Figure 2. cAMP dynamics with soluble and membrane bound actuators and reporters. **A)** Kinetic model for (i) photoactivation of bPAC, (ii) cAMP production and degradation, and (iii) cAMP sensing. **B)** Predicted blue light impulse responses (Equation 1 in Methods S1) for activated bPAC (called bPAC*, blue) and cAMP (pink) fit to PF+bPAC data (averaged over n = 17 HEK cells, circles). Simulated traces are plotted with k_{rev}^{bPAC} = 0.05 s^{-1} and k_{PDE} = 0.0125 s^{-1} and normalized to the peak. **C)** Genetic constructs for spatial control of actuator and reporter. Left: soluble PF and soluble bPAC. Right: membrane bound PF (PF^m) and membrane bound bPAC (bPAC^m). See Fig. S2 for PF+bPAC^m and PF^m+bPAC. **D)** Confocal images of fixed HEK cells with either soluble or membrane bound PF or EGFP-bPAC. Scale bar: 10 µm. **E)** Mean fluorescence responses of HEK cells expressing each combination of soluble or membrane bound bPAC and PF. All traces normalized to peak. Single-cell traces were fit to the same expression as in (B), with k_{rev}^{bPAC} fixed within each construct and k_{PDE} allowed to vary between cells. Error bars represent SEM. Data for PF+bPAC are the same as in panel B. **F)** Extracted PDE rate constant for (left to right): PF+bPAC, PF^m+bPAC, PF+bPAC^m, and PF^m+bPAC^m (see Table 2). Boxes represent the interquartile range with the median denoted by the central line. All four conditions are not significantly different according to the Wilcoxon rank-sum test.

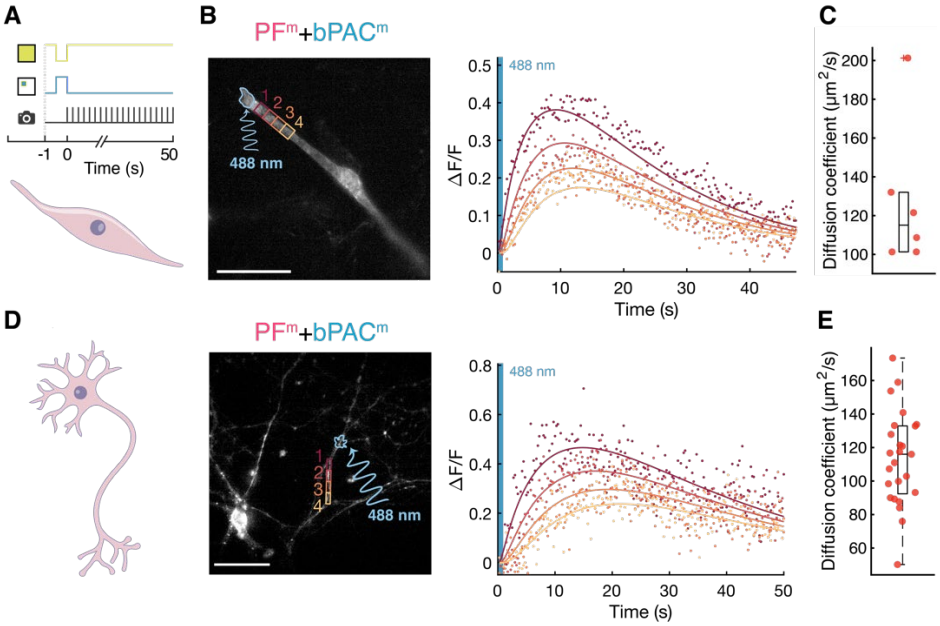

Figure 3. cAMP diffuses freely in MDCK cells and neurons.
A) Illumination protocol for patterned bPAC^m activation (blue, 0.5 s) followed by wide-field PF^m imaging (yellow). **B)** MDCK cell expressing PF^m and bPAC^m. 488 nm light was targeted to the indicated region (left). Traces of ΔF/F in the correspondingly colored regions were fit to the free diffusion model (D = 109 μm^2/s, right). Scale bar: 50 μm. **C)** cAMP diffusion coefficient in MDCK cells: D = 130 ± 40 μm^2/s (mean ± s.d., n = 6 measurements, 5 cells). **D)** Data from a **r**epresentative cultured neuron (D = 133 μm^2/s). Scale bar: 50 μm. **E)** cAMP diffusion coefficients in neurons: D = 110 ± 30 μm^2/s (mean ± s.d., n = 25 neurites in 8 cells). Boxes represent the interquartile range with the median denoted by the central line.

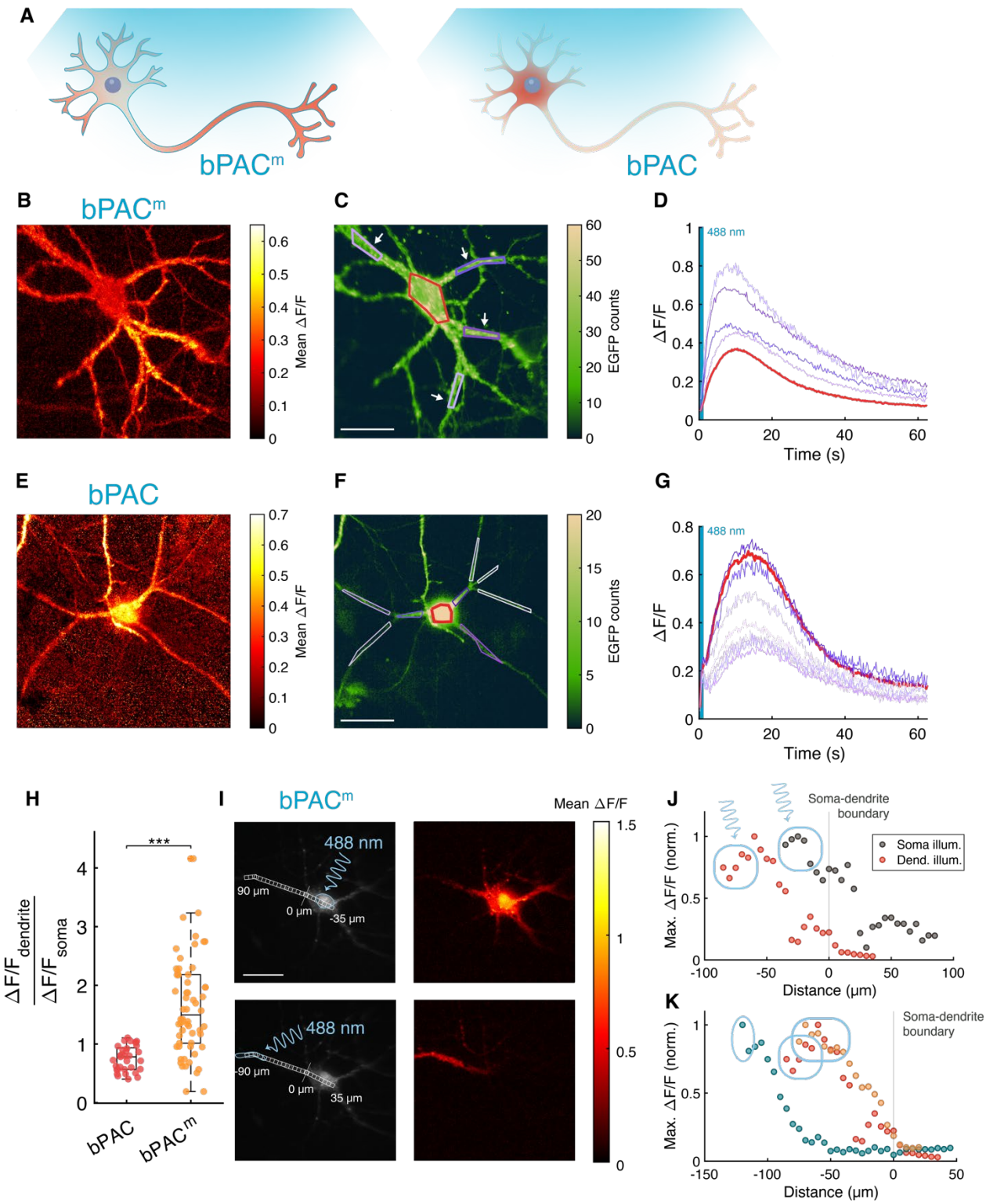

Figure 4. Membrane production and degradation cause heterogeneous cAMP distributions. A) Cartoon of a neuron expressing membrane-bound bPAC. Upon wide-area homogeneous blue light stimulation, cAMP accumulated preferentially in neurites due to a high surface-to-volume ratio and mixed bulk and membrane-localized degradation from PDEs. Soluble bPAC and the

same illumination profile resulted in preferential cAMP accumulation in the soma due to its low surface-to-volume ratio and hence slower rate of cAMP degradation. **B)** Mean PF^m fluorescence for the first 25 s in a PF^m+$bPAC^m$-expressing neuron following to a 0.5 s wide-area 488 nm light stimulus. The cAMP increase in the neurites was larger than in the cell body. Scale bar: 50 µm. **C)** EGFP-$bPAC^m$ image showing $bPAC^m$ distribution. **D)** PF^m ΔF/F in the soma (red) and neurites (purple). **E–G)** Same as **B–D** but for a neuron expressing PF^m+bPAC. **H)** Ratio of the peak ΔF/F in each dendrite scaled by the peak ΔF/F achieved in its corresponding soma. $N = 62$ dendrites and 6 cells for $bPAC^m$, and $n = 33$ dendrites and 6 cells for bPAC. *** p = 1.0e-8 (Wilcoxon rank-sum test). Boxes represent the interquartile range with the median denoted by the central line. **I)** Neurons expressing PF+$bPAC^m$ were subject to 0.5 s of 488 nm patterned illumination in the region circled (blue, either soma or dendrite). Right: Mean PF ΔF/F for the first 25 s. Scale bar: 50 µm. **J)** Maximum PF ΔF/F achieved in each region along the line denoted in (**I**), normalized by the peak value. For each stimulus location, distance was measured relative to the blue illumination spot, and offset so zero corresponds to the boundary between the soma and dendrite. Soma-produced cAMP permeated the dendrites, but dendrite-produced cAMP did not change cAMP concentration in the soma. **K)** Maximum PF ΔF/F achieved along the dendrite-soma axis for dendrite-targeted illumination in different cells ($n = 3$). Distance is offset so the soma-dendrite boundary is at 0. Blue circles indicate illumination spots. In (**J**) and (**K**) data are discretized into in 5 µm segments.

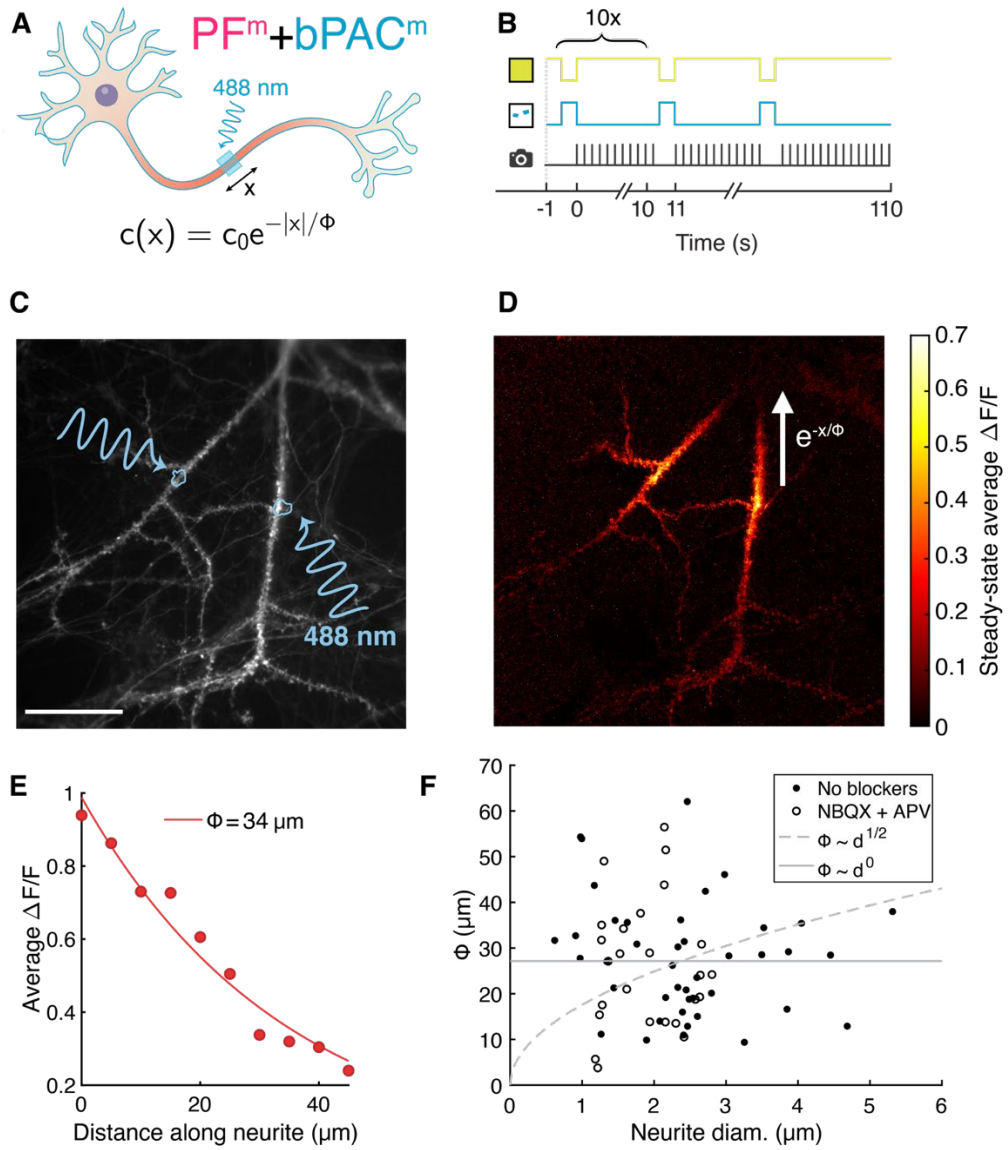

Figure 5. cAMP length constants in neurites.

A) Cartoon of localized cAMP production in a neurite. The steady-state cAMP concentration profile is a decaying exponential in space. The Thiele length, ϕ, is the cAMP length scale and depends on the balance between diffusion and degradation. **B)** Illumination protocol comprising interlaced localized blue light stimulation and wide-field yellow light imaging. **C)** PF^m+$bPAC^m$-expressing neurons were subject to targeted bPAC stimulation and cAMP profile was imaged at steady state. Scale bar: 50 µm. **D)** Mean PF ΔF/F after steady state was achieved. **E)** Mean ΔF/F along the neurite, with the illumination region at position 0. Space is discretized in 4 µm segments. An exponential fit yielded $1/\phi = (0.029 \pm 0.005)$ μm^{-1}. **F)** Thiele length, ϕ, plotted against neurite diameter shows a large variability between neurites, both with and without synaptic blockers (10 µM NBQX, 50 µM D-APV). Lines show theoretical predictions for purely soluble PDE activity ($\phi \sim d^0$) and purely membrane-bound PDE activity ($\phi \sim d^{1/2}$), where d is the neurite diameter. $N = 67$ neurites, 19 cells, 7 dishes.

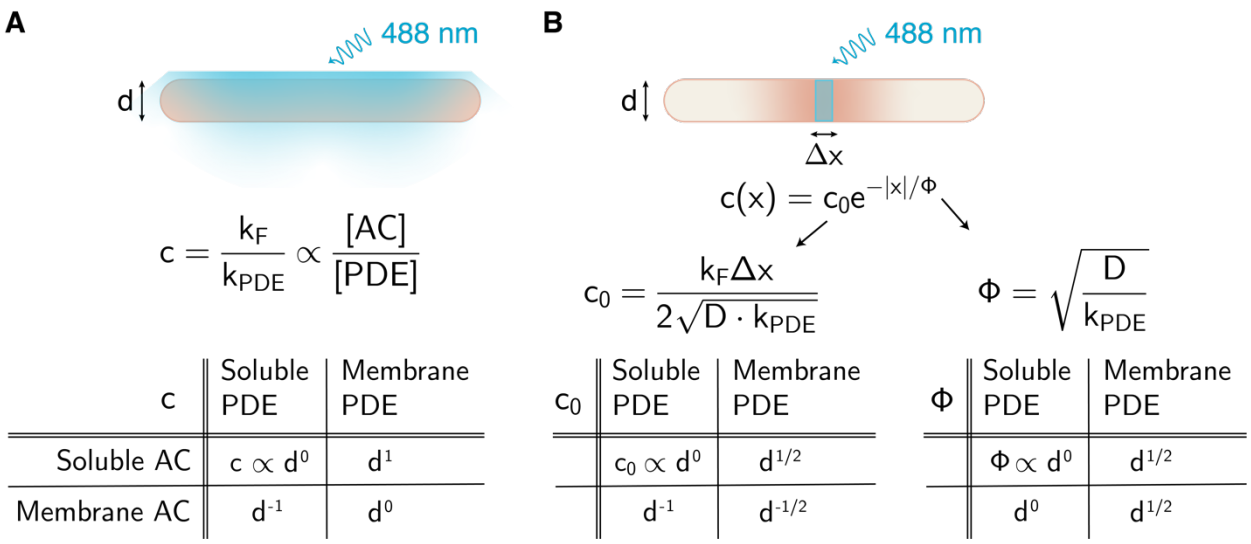

c	Soluble PDE	Membrane PDE
Soluble AC	$c \propto d^0$	d^1
Membrane AC	d^{-1}	d^0

c_0	Soluble PDE	Membrane PDE
	$c_0 \propto d^0$	$d^{1/2}$
	d^{-1}	$d^{-1/2}$

Φ	Soluble PDE	Membrane PDE
	$\Phi \propto d^0$	$d^{1/2}$
	d^0	$d^{1/2}$

Figure 6. Scaling of cAMP concentration and transport with tube diameter depend on enzyme localization.

A) Cartoon of wide-area homogeneous bPAC activation in a tube with diameter *d*. The steady state cAMP concentration depends on the ratio between AC and PDE effective concentrations. Effective concentrations of membrane-bound AC or PDE scale as d^{-1}; effective concentrations of soluble enzymes scale as d^0. **B)** Cartoon showing localized bPAC activation in a region with small width Δx. The concentration follows a decaying exponential in space, and both the peak concentration c_0 and the length scale ϕ can vary with tube diameter depending on enzyme localization.

Materials and Methods

Genetic constructs

The genes were cloned into a second-generation lentiviral backbone with cytomegalovirus (CMV) promoter using standard Gibson Assembly. Briefly, the vector was linearized by double digestion using restriction enzymes (New England Biolabs, Ipswich, MA) and purified by the GeneJET gel extraction kit (ThermoFisher, Waltham, MA). DNA fragments were generated by PCR amplification and then fused with the backbones using NEBuilder HiFi DNA assembly kit (New England Biolabs). Constructs were transformed and amplified in NEB 5-alpha Competent E. coli (New England Biolabs), and isolated using GeneJET miniprep kit (Thermo Scientific, Waltham, MA). All plasmids were verified by sequencing (GeneWiz, Cambridge, MA). The plasmids used in this work are listed in Table 2 and are available at Addgene.

Cell culture and expression

Human embryonic kidney (HEK293T) cells (ATCC CRL-11268) were cultured and transfected following standard protocols. Briefly, HEK293T cells were grown at 37 °C, 5% CO_2, in Dulbecco's modified Eagle's medium (DMEM) supplemented with 10% fetal bovine serum (FBS), penicillin (100 U/mL), and streptomycin (100 µg/mL). For maintaining or expanding the cell culture, we used tissue culture (TC)-treated culture dishes for optimum growth of anchorage-dependent cells (Corning). For imaging, cells were plated on poly-D-lysine (PDL)-coated glass-bottomed dishes (Cellvis, Cat.# D35-14-1.5-N). 2 µg of plasmid DNA was transfected per dish

using Transit 293T (Mirus) following the manufacturer's instructions and measured at least 48 h later.

Madin-Darby canine kidney (MDCK) cells were cultured at 37 °C, 5% CO_2, in DMEM supplemented with 10% FBS, penicillin (100 U/mL), and streptomycin (100 µg/mL). We used the TC-treated culture dishes (Corning) for maintaining or expanding the cell culture, and uncoated glass-bottomed dishes for imaging (Cellvis, Cat.# D35-14-1.5-N). MDCK cells were transduced with 200 µL lentivirus.

Primary E18 rat hippocampal neurons (fresh, never frozen, BrainBits #SDEHP) were dissociated following vendor protocols and plated in PDL and laminin-coated glass bottom dishes. Neurons (21k/cm^2) were cocultured with primary rat glia (27k/cm^2) to improve cell health and maturation. Neurons were transduced after 5-10 days in culture with 200 µL of low-titer lentivirus-containing media.

Lentivirus production

Lentivirus preparations were made in house. HEK293T cells were grown to 80% confluence in a 35 mm dish. Fresh DMEM was exchanged 1 to 2 hours before DNA transfection. Transfer plasmid (0.9 µg), second generation packaging plasmid psPAX2 (0.9 µg; Addgene #12260), and envelope plasmid VSV-G (0.6 µg; Addgene #12259) were mixed with reduced-serum Minimal Essential Medium (Opti-MEM; 250 µL). The mixture was vortexed briefly and incubated at room temperature for 20 min. The mixture was then added dropwise to the dish of HEK293T cells and incubated for 48 hours. Cell culture supernatant was collected and filtered using a 0.45-µm syringe filter and aliquoted for storage at −80°C.

Imaging

Before optical stimulation and imaging, cultured cells in 35 mm dishes were washed twice with 1 mL extracellular (XC) buffer containing (in mM): 125 NaCl, 2.5 KCl, 2 $CaCl_2$, 1 $MgCl_2$, 15 HEPES, 25 sucrose (adjusted to pH 7.3 and 304 mOsm L^{-1}) and then incubated with 1 mL XC buffer warmed to 37 °C. Samples were imaged at room temperature.

Experiments were conducted on a home-built inverted fluorescence microscope equipped with 405 nm, 488 nm, 532 nm, 561 nm, 594 nm, and 640 nm laser lines and a scientific complementary metal-oxide semiconductor (sCMOS) camera (Hamamatsu ORCA-Flash 4.0). Beams from lasers were combined using dichroic mirrors and sent through an acousto-optic tunable filter (AOTF; Gooch and Housego TF525-250-6-3-GH18A) for temporal modulation of intensity of each wavelength. The beams were then expanded and sent either to a DMD (Vialux, V-7000 UV, 9515) for spatial modulation or sent directly into the microscope (to avoid power losses associated with the DMD). The beams were focused onto the back-focal plane of a 60×/1.2-NA (numerical aperture) water-immersion objective (Olympus UIS2 UPlanSApo ×60/1.20W) or a 20×/0.75-NA objective (Olympus UIS2 UPlanSApo ×20/0.75). Fluorescence emission was separated from laser excitation using a dichroic mirror (488/561/633). Imaging of Pink Flamindo fluorescence was performed with a 561 nm laser at an illumination intensity of 7.4 mW mm^{-2} and imaged with a 596/40 emission filter. Stimulation of bPAC was performed with 488 nm laser at illumination intensities of 19–283 µW mm^{-2}. Photoactivation of paGFP was performed with 405 nm laser for 10 seconds. Imaging of EGFP fluorescence was a terminal experiment (due to concurrent bPAC

activation) with 488 nm laser at an illumination intensity of 21 μW mm^{-2} and a 532/50 emission filter.

Confocal imaging of fixed cells was performed on a Zeiss LSM 980 microscope. Cells were fixed with 5% paraformaldehyde and shielded from light until imaging.

Modeling and analysis

Data were analyzed with custom software (MATLAB). All videos are collected at 4 frames per second. ΔF/F was computed by taking the cell-averaged raw fluorescence intensities after subtracting the camera and background counts, then dividing by the time-averaged baseline fluorescence. For diffusion and Thiele length analyses, the background was computed by taking the 20th percentile of fluorescence intensity for pixels in a dark region of the field of view during imaging. For kinetics calculations, the background was computed by taking the mode of all pixels during the baseline period after subtracting camera dark counts. For videos and time-averaged images of the entire field of view, the background was not subtracted for visualization purposes. Time-averaged neurite length scale images such as in Fig. 5 were 2D median filtered with a kernel size of 3 pixels. Statistical tests are done with the Wilcoxon rank-sum test.

Kinetics, diffusion, and neuron length scale modeling as well as further information about analysis can be found in the Supplemental Information.

Tables

Table 1. HEK293T cell pharmacology

Condition	Number of cells	Number of exp. replicates
PF+bPAC	40	3
+ 0.1 μM Rolipram	19	2
+ 10 μM MR-L2	39	2
PF only	42	2

Table 2. Genetic constructs in this study

Construct name	**Full construct**	**Reference**
PF+bPAC	pLenti-CMV-Pink Flamindo-p2a-bPAC	Addgene #202716
PF^m +bPAC	pLenti-CMV-Myr-Pink Flamindo-p2a-EGFP-bPAC	Addgene #202717
PF+$bPAC^m$	pLenti-CMV-Pink Flamindo-p2a-paGFP-bPAC-CAAX	Addgene #202718
PF^m +$bPAC^m$	pLenti-CMV-Myr-Pink Flamindo-p2a-EGFP-bPAC-CAAX	Addgene #202719
PF	Pink Flamindo	Addgene #102356
bPAC	bPAC	Addgene #85468
PF^m	pLenti-CMV-Myr-Pink Flamindo	Addgene #204669
paGFP-bPAC	pLenti-CMV-paGFP-bPAC	Addgene #204670
paGFP-$bPAC^m$	pLenti-CMV-paGFP-bPAC-CAAX	Addgene #204671

Table 3. Kinetic parameters of cAMP-SITE constructs in HEK293T cells.

Construct	k_{PDE} (s^{-1})	k_{rev}^{bPAC}(s^{-1})	Number of cells	Number of exp. replicates
PF+bPAC	0.014 ± 0.007	0.050 ± 0.017	17	3
PF^m +bPAC	0.013 ± 0.008	0.051 ± 0.023	16	2
PF+$bPAC^m$	0.014 ± 0.008	0.050 ± 0.023	19	2
PF^m +$bPAC^m$	0.016 ± 0.006	0.069 ± 0.018	64	2

References

1. D. Yang, Q. Zhou, V. Labroska, S. Qin, S. Darbalaei, Y. Wu, E. Yuliantie, L. Xie, H. Tao, J. Cheng, Q. Liu, S. Zhao, W. Shui, Y. Jiang, M.-W. Wang, G protein-coupled receptors: structure- and function-based drug discovery. *Sig Transduct Target Ther*. **6**, 7 (2021).

2. L. L. Brunton, J. S. Hayes, S. E. Mayer, Hormonally specific phosphorylation of cardiac troponin I and activation of glycogen phosphorylase. *Nature*. **280**, 78–80 (1979).

3. J. S. Hayes, L. L. Brunton, S. E. Mayer, Selective activation of particulate cAMP-dependent protein kinase by isoproterenol and prostaglandin E1. *Journal of Biological Chemistry*. **255**, 5113–5119 (1980).

4. Q. N. Mai, T.-Y. Lin, H. Zhang, E. Wilson, H.-C. Chien, S. W. Yee, K. M. Giacomini, J. E. Olgin, R. Irannejad, "GPCR-dependent spatiotemporal cAMP generation confers functional specificity in cardiomyocytes and cardiac responses" (preprint, Cell Biology, 2022), , doi:10.1101/2022.07.13.499965.

5. M. Zaccolo, T. Pozzan, Discrete Microdomains with High Concentration of cAMP in Stimulated Rat Neonatal Cardiac Myocytes. *Science*. **295**, 1711–1715 (2002).

6. M. E. Truong, S. Bilekova, S. P. Choksi, W. Li, L. J. Bugaj, K. Xu, J. F. Reiter, Vertebrate cells differentially interpret ciliary and extraciliary cAMP. *Cell*. **184**, 2911-2926.e18 (2021).

7. A. D. White, K. A. Peña, L. J. Clark, C. S. Maria, S. Liu, F. G. Jean-Alphonse, J. Y. Lee, S. Lei, Z. Cheng, C.-L. Tu, F. Fang, N. Szeto, T. J. Gardella, K. Xiao, S. H. Gellman, I. Bahar, I. Sutkeviciute, W. Chang, J.-P. Vilardaga, Spatial bias in cAMP generation determines biological responses to PTH type 1 receptor activation. *Sci. Signal.* **14**, eabc5944 (2021).

8. C. P. O'Banion, B. M. Vickerman, L. Haar, D. S. Lawrence, Compartmentalized cAMP Generation by Engineered Photoactivated Adenylyl Cyclases. *Cell Chemical Biology*. **26**, 1393-1406.e7 (2019).

9. V. O. Nikolaev, A. Moshkov, A. R. Lyon, M. Miragoli, P. Novak, H. Paur, M. J. Lohse, Y. E. Korchev, S. E. Harding, J. Gorelik, b2-Adrenergic Receptor Redistribution in Heart Failure Changes cAMP Compartmentation. **327**, 6 (2010).

10. M. Bathe-Peters, P. Gmach, H.-H. Boltz, J. Einsiedel, M. Gotthardt, H. Hübner, P. Gmeiner, M. J. Lohse, P. Annibale, Visualization of β-adrenergic receptor dynamics and

differential localization in cardiomyocytes. *Proc. Natl. Acad. Sci. U.S.A.* **118**, e2101119118 (2021).

11. D. Ohadi, P. Rangamani, Geometric Control of Frequency Modulation of cAMP Oscillations due to Calcium in Dendritic Spines. *Biophysical Journal*. **117**, 1981–1994 (2019).

12. S. S Mogre, A. I. Brown, E. F. Koslover, Getting around the cell: physical transport in the intracellular world. *Phys. Biol.* **17**, 061003 (2020).

13. Z. Yang, E. F. Koslover, Diffusive Exit Rates Through Pores in Membrane-Enclosed Structures (2022), doi:10.48550/ARXIV.2210.14357.

14. I. Maiellaro, M. J. Lohse, R. J. Kittel, D. Calebiro, cAMP Signals in Drosophila Motor Neurons Are Confined to Single Synaptic Boutons. *Cell Reports*. **17**, 1238–1246 (2016).

15. A. Govindarajan, I. Israely, S.-Y. Huang, S. Tonegawa, The dendritic branch is the preferred integrative unit for protein synthesis-dependent LTP. *Neuron*. **69**, 132–146 (2011).

16. L. R. V. Castro, N. Gervasi, E. Guiot, L. Cavellini, V. O. Nikolaev, D. Paupardin-Tritsch, P. Vincent, Type 4 phosphodiesterase plays different integrating roles in different cellular domains in pyramidal cortical neurons. *J Neurosci*. **30**, 6143–6151 (2010).

17. J. Wagner, J. Keizer, Effects of rapid buffers on Ca2+ diffusion and Ca2+ oscillations. *Biophysical Journal*. **67**, 447–456 (1994).

18. M. Gabso, E. Neher, M. E. Spira, Low Mobility of the Ca2+ Buffers in Axons of Cultured Aplysia Neurons. *Neuron*. **18**, 473–481 (1997).

19. A. Zador, C. Koch, Linearized models of calcium dynamics: formal equivalence to the cable equation. *J. Neurosci.* **14**, 4705–4715 (1994).

20. C. Koch, *Biophysics of computation: information processing in single neurons* (Oxford university press, 2004).

21. A. Bock, P. Annibale, C. Konrad, A. Hannawacker, S. E. Anton, I. Maiellaro, U. Zabel, S. Sivaramakrishnan, M. Falcke, M. J. Lohse, Optical Mapping of cAMP Signaling at the Nanometer Scale. *Cell*. **182**, 1519-1530.e17 (2020).

22. K. Omori, J. Kotera, Overview of PDEs and Their Regulation. *Circulation Research*. **100**, 309–327 (2007).

23. S. E. Anton, C. Kayser, I. Maiellaro, K. Nemec, J. Möller, A. Koschinski, M. Zaccolo, P. Annibale, M. Falcke, M. J. Lohse, A. Bock, Receptor-associated independent cAMP nanodomains mediate spatiotemporal specificity of GPCR signaling. *Cell*. **185**, 1130-1142.e11 (2022).

24. S. R. Agarwal, C. E. Clancy, R. D. Harvey, Mechanisms Restricting Diffusion of Intracellular cAMP. *Sci Rep*. **6**, 19577 (2016).

25. B. Bacskai, B. Hochner, M. Mahaut-Smith, Adams, B. Kaang, E. Kandel, R. Tsien, Spatially resolved dynamics of cAMP and protein kinase A subunits in Aplysia sensory neurons. *Science*. **260**, 222–226 (1993).

26. M. Stierl, P. Stumpf, D. Udwari, R. Gueta, R. Hagedorn, A. Losi, W. Gärtner, L. Petereit, M. Efetova, M. Schwarzel, T. G. Oertner, G. Nagel, P. Hegemann, Light Modulation of Cellular cAMP by a Small Bacterial Photoactivated Adenylyl Cyclase, bPAC, of the Soil Bacterium Beggiatoa*♦. *Journal of Biological Chemistry*. **286**, 1181–1188 (2011).

27. K. Harada, M. Ito, X. Wang, M. Tanaka, D. Wongso, A. Konno, H. Hirai, H. Hirase, T. Tsuboi, T. Kitaguchi, Red fluorescent protein-based cAMP indicator applicable to optogenetics and in vivo imaging. *Sci Rep*. **7**, 7351 (2017).

28. J. H. Kim, S.-R. Lee, L.-H. Li, H.-J. Park, J.-H. Park, K. Y. Lee, M.-K. Kim, B. A. Shin, S.-Y. Choi, High Cleavage Efficiency of a 2A Peptide Derived from Porcine Teschovirus-1 in Human Cell Lines, Zebrafish and Mice. *PLoS ONE*. **6**, e18556 (2011).

29. R. J. Duronio, E. Jackson-Machelski, R. O. Heuckeroth, P. O. Olins, C. S. Devine, W. Yonemoto, L. W. Slice, S. S. Taylor, J. I. Gordon, Protein N-myristoylation in Escherichia coli: reconstitution of a eukaryotic protein modification in bacteria. *Proc. Natl. Acad. Sci. U.S.A.* **87**, 1506–1510 (1990).

30. R. Lindner, E. Hartmann, M. Tarnawski, A. Winkler, D. Frey, J. Reinstein, A. Meinhart, I. Schlichting, Photoactivation Mechanism of a Bacterial Light-Regulated Adenylyl Cyclase. *Journal of Molecular Biology*. **429**, 1336–1351 (2017).

31. C. Villarruel, P. S. Aguilar, S. Ponce Dawson, High rates of calcium-free diffusion in the cytosol of living cells. *Biophysical Journal*. **120**, 3960–3972 (2021).

32. A. I. García-Pérez, E. A. López-Beltrán, P. Klüner, J. Luque, P. Ballesteros, S. Cerdán, Molecular Crowding and Viscosity as Determinants of Translational Diffusion of Metabolites in Subcellular Organelles. *Archives of Biochemistry and Biophysics*. **362**, 329–338 (1999).

33. C. Steegborn, Structure, mechanism, and regulation of soluble adenylyl cyclases — similarities and differences to transmembrane adenylyl cyclases. *Biochimica et Biophysica Acta (BBA) - Molecular Basis of Disease*. **1842**, 2535–2547 (2014).

34. A. M. Ellisdon, M. L. Halls, Compartmentalization of GPCR signalling controls unique cellular responses. *Biochemical Society Transactions*. **44**, 562–567 (2016).

35. D. Calebiro, V. O. Nikolaev, M. C. Gagliani, T. De Filippis, C. Dees, C. Tacchetti, L. Persani, M. J. Lohse, Persistent cAMP-Signals Triggered by Internalized G-Protein–Coupled Receptors. *PLoS Biol*. **7**, e1000172 (2009).

36. M. Conti, S.-L. C. Jin, "The Molecular Biology of Cyclic Nucleotide Phosphodiesterases" in *Progress in Nucleic Acid Research and Molecular Biology* (Elsevier, 1999; https://linkinghub.elsevier.com/retrieve/pii/S0079660308607187), vol. 63, pp. 1–38.

37. B. E. Blackman, K. Horner, J. Heidmann, D. Wang, W. Richter, T. C. Rich, M. Conti, PDE4D and PDE4B Function in Distinct Subcellular Compartments in Mouse Embryonic Fibroblasts. *Journal of Biological Chemistry*. **286**, 12590–12601 (2011).

38. D. Paes, S. Hermans, D. van den Hove, T. Vanmierlo, J. Prickaerts, A. Carlier, Computational investigation of the dynamic control of cAMP signaling by PDE4 isoform types. *Biophys J*. **121**, 2693–2711 (2022).

39. E. W. Thiele, Relation between Catalytic Activity and Size of Particle. *Ind. Eng. Chem.* **31**, 916–920 (1939).

40. B. Hille, *Ion channels of excitable membranes* (Sinauer, Sunderland, Mass, 3rd ed., 2001).

41. J. D. Wong-Campos, P. Park, H. C. Davis, Y. Qi, H. Tian, D. G. Itkis, D. Kim, J. B. Grimm, S. E. Plutkis, L. Lavis, A. E. Cohen, Voltage dynamics of dendritic integration and back-propagation in vivo (2023), doi:10.1101/2023.05.25.542363.

42. P. Park, D. Wong-Campos, D. G. Itkis, Y. Qi, H. Davis, J. B. Grimm, S. E. Plutkis, L. Lavis, A. E. Cohen, Dendritic voltage imaging reveals biophysical basis of associative plasticity rules (2023), p. 2023.06.02.543490, , doi:10.1101/2023.06.02.543490.

43. I. Derényi, F. Jülicher, J. Prost, Formation and Interaction of Membrane Tubes. *Phys.Rev.Lett.* **88**, 238101 (2002).

44. G. C. Brown, B. N. Kholodenko, Spatial gradients of cellular phospho-proteins. *FEBS Letters*. **457**, 452–454 (1999).

45. B. N. Kholodenko, Cell-signalling dynamics in time and space, 12 (2006).

46. J. Meyers, J. Craig, D. J. Odde, Potential for Control of Signaling Pathways via Cell Size and Shape. *Current Biology*. **16**, 1685–1693 (2006).

47. S. R. Neves, P. Tsokas, A. Sarkar, E. A. Grace, P. Rangamani, S. M. Taubenfeld, C. M. Alberini, J. C. Schaff, R. D. Blitzer, I. I. Moraru, R. Iyengar, Cell Shape and Negative Links in Regulatory Motifs Together Control Spatial Information Flow in Signaling Networks. *Cell*. **133**, 666–680 (2008).

48. C. Chen, T. Nakamura, Y. Koutalos, Cyclic AMP Diffusion Coefficient in Frog Olfactory Cilia. *Biophysical Journal*. **76**, 2861–2867 (1999).

49. V. O. Nikolaev, M. Bünemann, E. Schmitteckert, M. J. Lohse, S. Engelhardt, Cyclic AMP Imaging in Adult Cardiac Myocytes Reveals Far-Reaching β_1-Adrenergic but Locally Confined β_2-Adrenergic Receptor–Mediated Signaling. *Circulation Research*. **99**, 1084–1091 (2006).

50. A. A. Choi, L. Xiang, W. Li, K. Xu, *J. Am. Chem. Soc.*, in press, doi:10.1021/jacs.3c00597.

51. J. Z. Zhang, T.-W. Lu, L. M. Stolerman, B. Tenner, J. R. Yang, J.-F. Zhang, M. Falcke, P. Rangamani, S. S. Taylor, S. Mehta, J. Zhang, Phase Separation of a PKA Regulatory Subunit Controls cAMP Compartmentation and Oncogenic Signaling. *Cell*. **182**, 1531-1544.e15 (2020).

52. V. Agus, H. Janovjak, Optogenetic methods in drug screening: technologies and applications. *Current Opinion in Biotechnology*. **48**, 8–14 (2017).

53. T. Gregor, E. F. Wieschaus, A. P. McGregor, W. Bialek, D. W. Tank, Stability and Nuclear Dynamics of the Bicoid Morphogen Gradient. *Cell*. **130**, 141–152 (2007).

54. A. Datta, S. Ghosh, J. Kondev, How to assemble a scale-invariant gradient. *eLife*. **11**, e71365 (2022).

55. X. Zhou, S. Mehta, J. Zhang, Genetically Encodable Fluorescent and Bioluminescent Biosensors Light Up Signaling Networks. *Trends in Biochemical Sciences*. **45**, 889–905 (2020).

56. D. L. Schmitt, S. Mehta, J. Zhang, Study of spatiotemporal regulation of kinase signaling using genetically encodable molecular tools. *Current Opinion in Chemical Biology*. **71**, 102224 (2022).

57. M. Z. Lin, M. J. Schnitzer, Genetically encoded indicators of neuronal activity. *Nat.Neurosci.* **19**, 1142–1153 (2016).

58. L. Wu, A. Dong, L. Dong, S.-Q. Wang, Y. Li, PARIS, an optogenetic method for functionally mapping gap junctions. *eLife*. **8**, e43366 (2019).

59. C. I. Massengill, L. Bayless-Edwards, C. C. Ceballos, E. R. Cebul, J. Cahill, A. Bharadwaj, E. Wilson, M. Qin, M. R. Whorton, I. Baconguis, B. Ye, T. Mao, H. Zhong, Sensitive genetically encoded sensors for population and subcellular imaging of cAMP in vivo. *Nat Methods*. **19**, 1461–1471 (2022).

60. C. I. Massengill, J. Day-Cooney, T. Mao, H. Zhong, Genetically encoded sensors towards imaging cAMP and PKA activity in vivo. *Journal of Neuroscience Methods*. **362**, 109298 (2021).

Supplemental Figures

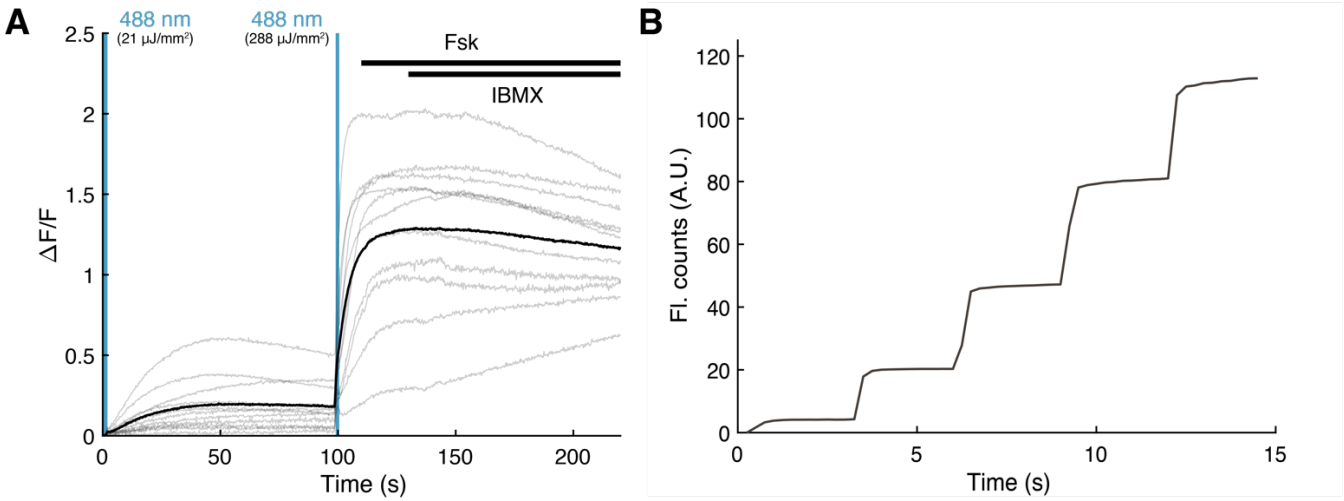

Figure S1. Characterization of PF+bPAC cAMP-SITE.
A) Strong bPAC activation saturated the PF reporter. In HEK cells expressing bPAC+PF, a low-intensity 0.5 s pulse of 488 nm light activated bPAC and evoked a PF response. At 100 s, a high-intensity 0.5 s pulse of 488 nm light evoked a larger PF response. After 10 s we added forskolin (final concentration 100 µM), then IBMX (final concentration 200 µM). These drugs did not further increase the PF response, implying saturation of the PF reporter. **B)** Yellow light did not activate bPAC. HEK cells expressing bPAC+PF were exposed to step-wise increases of 561 nm light, from 2 mW/mm^2 to 10 mW/mm^2. The PF fluorescence showed step-wise increases proportional to illumination intensity. Absence of slow PF transient responses confirmed negligible changes in cAMP concentration during this protocol (n = 15 cells).

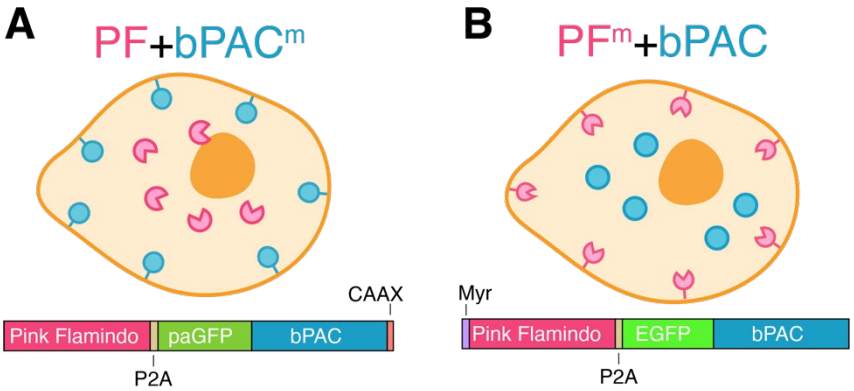

Figure S2. cAMP-SITE constructs with mixed membrane localization.
A) Soluble PF and membrane-bound bPAC. **B)** Membrane-bound PF and soluble bPAC.

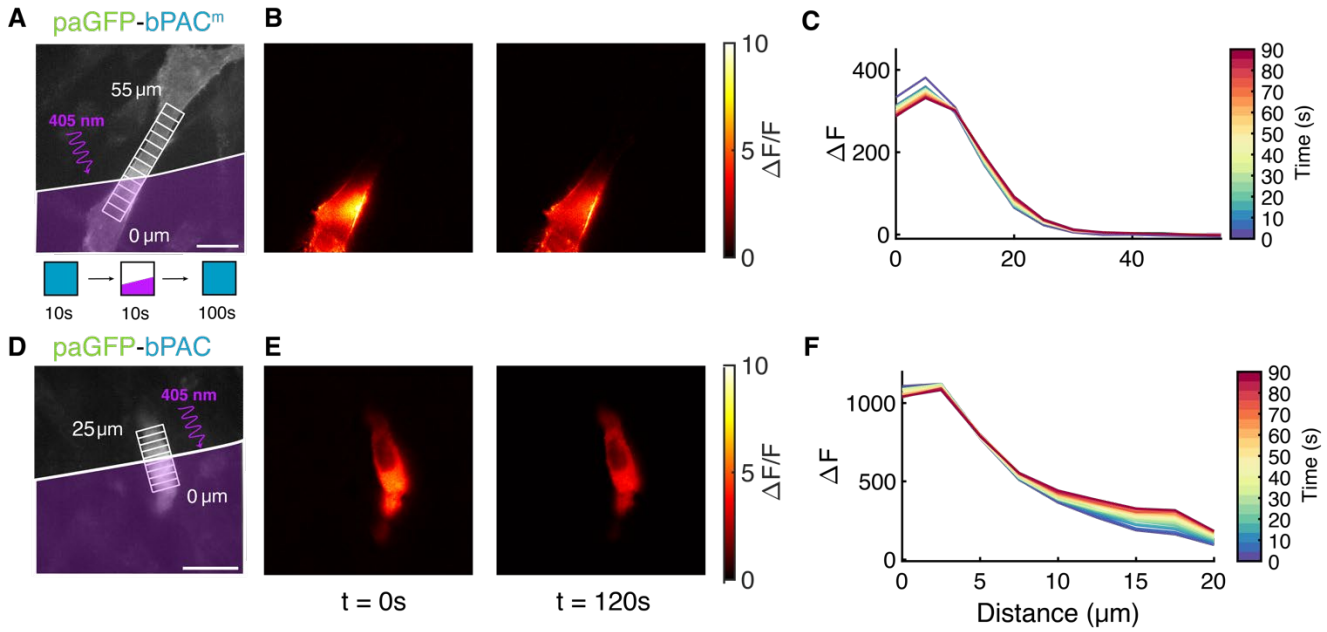

Figure S3. Photoactivation probes diffusion of membrane-bound and soluble bPAC.
A) paGFP tagged to bPAC^{m} was activated with purple (405 nm) light in a subcellular region for 10 s. GFP fluorescence was recorded with blue (488 nm) light. Scale bar: 20 µm. **B)** Images of GFP ΔF/F. Left: at t = 0 (immediately after the end of stimulation with purple light). Right: t = 120 s. **C)** ΔF for each region in **A** color-coded by time from t = 0 to t = 90 s. **D–F)** Same as **A–C** but for soluble bPAC.

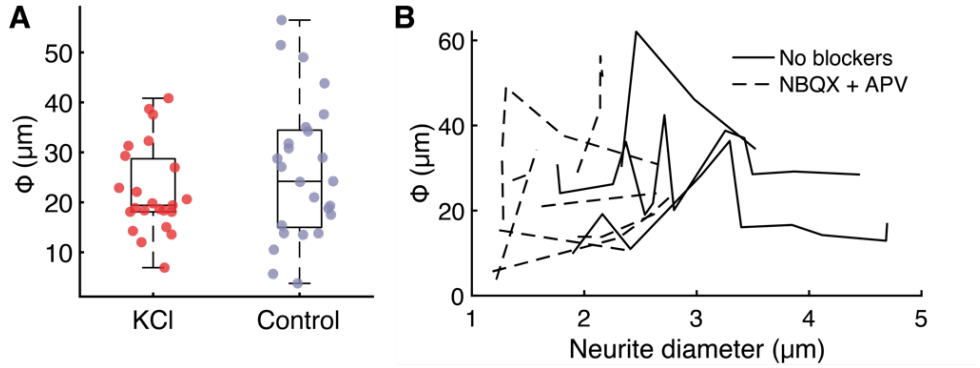

Figure S4. Neither depolarization nor neurite diameter affect cAMP length-scale in neurons.
A) Neurons in 50 mM KCl media (n = 23 neurites, ϕ = 22 ± 8.9 µm, mean ± s.d.) did not have significantly different cAMP length scales compared to those in the control group with 10 µM NBQX and 50 µM D-APV (n = 25 neurites, ϕ = 26 ± 14 µm, mean ± s.d.), Wilcoxon rank-sum test, p = 0.42. Boxes represent the interquartile range with the median denoted by the central line. **B)** cAMP length scale plotted against neurite diameter, with lines denoting neurites from the same cell.